MOX–Report No. 15/2014

Anisotropic mesh and time step adaptivity for solute transport modeling in porous media

Bahman Esfandiar, Giovanni Porta, Simona Perotto, Alberto Guadagnini

MOX, Dipartimento di Matematica "F. Brioschi"
Politecnico di Milano, Via Bonardi 9 - 20133 Milano (Italy)

mox@mate.polimi.it http://mox.polimi.it

Anisotropic mesh and time step adaptivity for solute transport modeling in porous media*

Bahman Esfandiar[♯], Giovanni Porta[♯], Simona Perotto[♭], Alberto Guadagnini[♯]

May 2, 2014

[♯] Dipartimento di Ingegneria Civile ed Ambientale, Politecnico di Milano
[♭] MOX– Modellistica e Calcolo Scientifico
Dipartimento di Matematica "F. Brioschi", Politecnico di Milano
Piazza Leonardo da Vinci 32, 20133 Milano, Italy
{bahman.esfandiar,giovanni.porta}@polimi.it
{simona.perotto,alberto.guadagnini}@polimi.it

Keywords: space-time adaptivity, anisotropic meshes, advection-dispersion equations.

AMS Subject Classification: 65M50, 65M60, 65M15

Abstract

We assess the impact of space-time mesh adaptivity on the modeling of solute transport in porous media. This approach allows an automatic selection of both the spatial mesh and the time step on the basis of a suitable recovery-based error estimator. In particular, we deal with an anisotropic control of the spatial mesh. The solver coupled with the adaptive module deals with an advection-dispersion equation to model the transport of dissolved species, which are assumed to be convected by a Darcy flow field. The whole solution-adaptation procedure is assessed through two-dimensional numerical tests. A numerical convergence analysis of the spatial mesh adaptivity is first performed by considering a test-case with analytical solution. Then, we validate the space-time adaptive procedure by reproducing a set of experimental observations associated with solute transport in a homogeneous sand pack. The accuracy and the efficiency of the methodology are discussed and numerical results are compared with those associated with fixed uniform space-time discretizations. This assessment shows that the proposed approach is robust and reliable. In particular, it allows us to obtain a significant improvement of the simulation quality of the early solute arrivals times at the outlet of the medium.

*This work has been supported by the Project MIUR "Innovative methods for water resources under hydro-climatic uncertainty scenarios", PRIN 2010/2011

1 Introduction

A wide set of physical processes involves transport of solutes in porous media. These include contamination of groundwater by inorganic and organic chemicals, petroleum generation and migration, reactive processes which can modify the properties of soil and rock formations. Several modeling techniques and analytical solutions are proposed in the literature, while a variety of algorithms and software packages have been developed for the numerical simulation of solute transport in the subsurface (see, e.g., [52, 3, 20]). Transport of solutes in porous media is typically modeled through an advection-dispersion equation, where the dispersive coefficient embeds the effects of molecular diffusion and hydrodynamic dispersion. The advective term results from a velocity field, which is typically assumed to obey Darcy's law.

Different examples of mesh adaptivity applied to fluid flow and solute transport in homogeneous and heterogeneous porous media are available in the literature (see, e.g., the review in [34]). In the context of flow simulation in heterogeneous media, the advantages resulting from an *a priori* refinement of an otherwise static mesh have been quantified in field scale flow simulation [36] as well as in transport problems [23]. In [30], a moving mesh algorithm for the modeling of a three-dimensional flow in the subsurface is proposed. A two-dimensional technique based on local refinement of hierarchical meshes is presented in [9]. The mesh adaptivity is here driven by an *a posteriori* error estimator for the energy norm. An example of anisotropic adaptivity is provided in [51], where a dynamic mesh adaptation for a reactive transport problem is proposed. The directional features of the solution are taken into account via local refinement/coarsening error indicators. In particular, the authors deal with structured and rectangular grids in a hierarchical framework.
Time step adaptivity has also been applied to the error control in the context of transient transport phenomena in porous media. These include density driven flows (e.g., [55, 54, 16]), flow in unsaturated media (e.g., [29]) and reactive transport processes [49].

In this contribution, we aim at combining mesh with time step adaptivity for modeling solute transport in porous media. To the best of our knowledge, this represents a first attempt in this applicative context. To maximize the advantages deriving from adapted meshes, we resort to an anisotropic mesh adaptivity (see, e.g., [12, 26, 45]). Size, orientation and shape of the elements are optimized to match the directional features of the problem at hand. We base our work on the methodology used in [47] for simulating unsteady shallow water problems. Here, the adaptive procedure relies on a recovery-based *a posteriori* estimator for the global (i.e., space–time) error. The contribution of space and time approximation errors is kept separated following, e.g., [11, 37, 38, 50] so that the space and the time discretization grids are sequentially and independently adapted. The spatial mesh adaptivity is grounded on the *a posteriori* error estimate proposed in [41], which essentially represents the anisotropic counterpart of the error estimator originally proposed by O.C. Zienkiewicz and J.Z. Zhu in [56]. This yields a computationally cheap, problem-independent error estimator, which has been already applied successfully to different two- and three-dimensional problem settings [46, 18, 39]. The time step adaptivity is derived through the recovery-based technique devised in [47].

This methodology allows us estimating the time approximation error upon relying on a higher-order local reconstruction of time derivatives. Finally, this paper is enriched by comparing the results provided by the proposed numerical approach with actual experimental data similar to those presented in [32]. This is a key contribution of this paper, and allows us discussing the impact of space-time adaptive simulation methodologies on the interpretation of experiments.

The paper is organized as follows. Section 2 introduces the flow and solute transport equations and the adopted finite-element discretization. In Section 3, we provide the reference anisotropic setting and define the recovery-based space-time error estimator. Section 4 provides the procedures adopted to predict the new space-time adapted mesh together with the coupling strategy used to combine the solver in Sect. 2.1 with the whole adaptive procedure. Finally, in Sect. 5 we deal with the numerical validation, by considering first a benchmark analytical test case and then by performing a comparison with the experimental results. A discussion with concluding remarks ends the paper.

2 Solute Transport Modeling

Solute transport in porous media is typically described through a standard advection-dispersion equation (ADE). While the transport phenomenon is intrinsically three-dimensional, we assume here that the variation of solute concentration along the vertical direction may be neglected. This approximation is typically acceptable in the context of the laboratory settings that we consider in this work and allows us casting the transport equation into a two-dimensional (planar) framework [3].
Let $\Omega \subset \mathbb{R}^2$ be a bounded polygonal domain with boundary $\partial\Omega$, and $[0,T]$ a time window of interest. The ADE reads

$$\frac{\partial C}{\partial t} + \nabla \cdot (\vec{v}C) - \nabla \cdot \left(\vec{D}\nabla C\right) = 0 \quad \text{in } \Omega \times (0,T], \tag{1}$$

where $C = C(\vec{x},t)$[mol/m^3] is the (unknown) vertically averaged solute concentration at location $\mathbf{x}$ and at time t, $\vec{v} = (v_1, v_2)^T$[m/s] is the fluid velocity and $\mathbf{D} = \{D_{ij}\}$ is the symmetric positive definite dispersion tensor. Following [3], this tensor is typically defined as

$$D_{ij} = (\alpha_T |\vec{v}| + D_m)\,\delta_{ij} + (\alpha_L - \alpha_T)\,\frac{v_i v_j}{\|\vec{v}\|_2} \quad \text{with } i,j = 1,2\,, \tag{2}$$

where α_T, α_L[m] are the transverse and the longitudinal dispersivity, respectively, δ_{ij} is Kronecker's delta symbol, D_m[m^2/s] is the molecular diffusion and $\|\mathbf{w}\|_2$ denotes the standard Euclidean norm of a generic vector $\mathbf{w} \in \mathbb{R}^2$. Equation (1) is completed with a suitable set of initial and boundary conditions which, in general, coincides with relations as

$$\begin{cases} C(\vec{x},0) = C_0(\vec{x}) & \text{for } \vec{x} \in \Omega, \\ C(\vec{x},t) = f_1(\vec{x},t) & \text{for } \vec{x} \in \Gamma_1,\ t \in (0,T], \\ -\left(\vec{D}\nabla C\right)\cdot\vec{n} = f_2(\vec{x},t) & \text{for } \vec{x} \in \Gamma_2,\ t \in (0,T], \\ \left(\vec{v}C - \vec{D}\nabla C\right)\cdot\vec{n} = f_3(\vec{x},t) & \text{for } \vec{x} \in \Gamma_3,\ t \in (0,T], \end{cases} \tag{3}$$

where Γ_1, Γ_2 and Γ_3, with $\cup_{i=1}^{3}\Gamma_i = \partial\Omega$, $\overset{\circ}{\Gamma}_i \cap \overset{\circ}{\Gamma}_j = \emptyset$, for $i, j = 1,2,3$ and $i \neq j$, represent a partition of the boundary $\partial\Omega$ associated with Dirichlet, Neumann and Robin boundary conditions, respectively, C_0 is the initial value of the solute concentration, f_i, with $i = 1,2,3$, are the boundary data, and $\vec{n}$ is the unit outward normal vector to $\partial\Omega$.
The velocity field $\mathbf{v}$ in (1) is typically obtained through the numerical approximation of the following equations

$$\begin{cases} \vec{v} = -\dfrac{k}{\mu\phi}\left(\nabla p + \rho g\vec{k}\right) & \text{for } \vec{x} \in \Omega, \\ \nabla \cdot \vec{v} = 0 & \text{for } \vec{x} \in \Omega, \\ \vec{v} \cdot \vec{n} = \psi & \text{for } \vec{x} \in \partial\Omega, \end{cases} \tag{4}$$

where p[Pa] is the pressure, g[m/s^2] is the gravity, $\mu > 0$[Pa·s] and $\rho > 0$[Kg/m^3] are the fluid viscosity and density, respectively, $k > 0$[m^2] is the porous medium permeability, $0 < \phi < 1$ is the porosity, ψ is a flux imposed on the domain boundary and $\mathbf{k}$ denotes the unit vector aligned with the vertical direction. In particular, we assume μ, ρ, k, ϕ real constants. Equation $(4)_1$ coincides with Darcy's law coupled with the continuity equation $(4)_2$, while equation $(4)_3$ models an imposed flux. Notice that, via the divergence theorem, we obtain $\int_{\partial\Omega} \psi\, ds = 0$. Since equations (4) are steady, we are assuming to deal with a time independent field $\vec{v}$ in (1).

2.1 The Finite Element Discretization

In this section, we provide the finite element formulation used to discretize problem (1)-(4). We first introduce the discretization of the flow problem (4) by resorting to a mixed two-field formulation (see, e.g., [35, 44, 15]). For this purpose, we consider the following function spaces

$$\begin{aligned} V = H(div,\Omega) &= \left\{\vec{v} \in [L^2(\Omega)]^2 \ : \ \nabla \cdot \vec{v} \in L^2(\Omega), \text{trace}(\vec{v} \cdot \vec{n}) = \psi \in H^{-1/2}(\partial\Omega)\right\}, \\ W = H_0(div,\Omega) &= \left\{\vec{w} \in [L^2(\Omega)]^2 \ : \ \nabla \cdot \vec{w} \in L^2(\Omega), \text{trace}(\vec{w} \cdot \vec{n}) = 0 \text{ on } \partial\Omega\right\}, \\ P = L^2_0(\Omega) &= \left\{p \in L^2(\Omega) \ : \ \int_\Omega p\, d\Omega = 0\right\}, \end{aligned} \tag{5}$$

where trace$(\cdot)$ denotes the standard trace operator. The demand on the average of p in P is due to the fact that the pressure field in (4) is involved in a gradient form. As a consequence, to guarantee the uniqueness of p, we have to constrain it with a condition. In practice, we specify the value of p at a certain point in Ω instead of implementing condition $\int_\Omega p\, d\Omega = 0$. For all the details concerning the spaces in (5), we refer to [6]. Thus, for given values of the physical parameters μ, k, ϕ, ρ and ψ, the weak formulation of (4) reads: find $\vec{v} \in V$ and $p \in P$ such that, for any $\vec{w} \in W$ and $q \in P$,

$$\int_\Omega \left(\frac{\mu\phi}{k}\vec{v} \cdot \vec{w} - p\nabla \cdot \vec{w} + \nabla \cdot \vec{v}q\right) d\Omega = -\int_\Omega \left(\rho g\vec{k} \cdot \vec{w}\right) d\Omega. \tag{6}$$

For sufficiently regular data, the weak formulation (6) is known to have a unique solution. To discretize problem (6), we introduce a conformal partition $\mathscr{T}_h = \{K\}$ of the

domain Ω into triangles K of diameter h_K [13]. Then, we define the spaces

$$V_h = \left\{ \vec{v}_h \in [L^2(\Omega)]^2 \ : \ \vec{v}_h\big|_K \in \mathbb{RT}_0(K), \forall K \in \mathscr{T}_h, \text{trace}(\vec{v}_h \cdot \vec{n}) = \psi_h \right\},$$
$$W_h = \left\{ \vec{w}_h \in [L^2(\Omega)]^2 \ : \ \vec{w}_h\big|_K \in \mathbb{RT}_0(K), \forall K \in \mathscr{T}_h, \text{trace}(\vec{w}_h \cdot \vec{n}) = 0 \right\},$$

where $\mathbb{RT}_0$ denotes the space of the zero-order Raviart–Thomas finite elements [6], while ψ_h is a piecewise constant approximation of the trace ψ. The space V_h is employed to discretize the velocity field, while W_h is used to discretize the test functions. This choice leads us to select the space

$$P_h = \left\{ p_h \in P \ : \ p_h\big|_K \in \mathbb{P}_0(K), \forall K \in \mathscr{T}_h \right\} \ ,$$

for the pressure, $\mathbb{P}_0$ being the set of the polynomials of degree zero. Thus, the $\mathbb{RT}_0 - \mathbb{P}_0$ discretization of problem (6) reads: find $\vec{v}_h \in V_h$ and $p_h \in P_h$ such that, for any $\vec{w}_h \in W_h$ and $q_h \in P_h$,

$$\sum_{K \in \mathscr{T}_h} \left\{ \int_K \left(\frac{\mu \phi}{k} \vec{v}_h \cdot \vec{w}_h - p_h \nabla \cdot \vec{w}_h + \nabla \cdot \vec{v}_h q_h \right) dK \right\} = \sum_{K \in \mathscr{T}_h} \left\{ - \int_K \left(\rho g \vec{k} \cdot \vec{w}_h \right) dK \right\}. \tag{7}$$

Notice that, the combination $\mathbb{RT}_0 - \mathbb{P}_0$ of shape functions for the velocity and pressure does satisfy the Babuška-Brezzi stability condition. Moreover, since we assume to deal with a steady velocity field, we solve problem (7) only once, for a prescribed set of data and before dealing with ADE (1).

The discretization of the ADE moves from the weak formulation of equation (1): for any $t \in (0,T]$, find $C(t) \in Z$ such that, for any $z \in Z$,

$$\int_\Omega \left(\frac{\partial C(t)}{\partial t} z + \left(\vec{D} \nabla C(t) - \vec{v} C(t) \right) \cdot \nabla z \right) d\Omega = 0, \tag{8}$$

where Z coincides with a subspace of the Sobolev space $H^1(\Omega)$, suitably modified to satisfy the essential boundary conditions assigned on $\partial\Omega$. On the other hand, the imposition of natural boundary conditions leads to modify accordingly the right-hand side in (8) by introducing suitable integral boundary terms.

The spatial discretization of (8) is obtained via a streamline upwind technique (see, e.g., [7]) to damp the spurious oscillations yielded by the standard Galerkin finite element approximation. Let $Z_h = \left\{ z_h \in C^0(\overline{\Omega}) \ : \ z_h\big|_K \in \mathbb{P}^1(K), \forall K \in \mathscr{T}_h \right\} \cap Z$ be the space of the affine finite elements associated with the partition $\mathscr{T}_h$. Thus, the streamline upwind finite element discretization of (8) is: for any $t \in (0,T]$, find $C_h(t) \in Z_h$ such that, for any $z_h \in Z_h$,

$$\begin{aligned} \sum_{K \in \mathscr{T}_h} \Big\{ & \int_K \Big(\frac{\partial C_h(t)}{\partial t} z_h + \left(\vec{D}_h \nabla C_h(t) - \vec{v}_h C_h(t) \right) \cdot \nabla z_h \Big) dK \\ & + Q_K \int_K \left(\vec{v}_h \cdot \nabla C_h(t) \right) \left(\vec{v}_h \cdot \nabla z_h \right) dK \Big\} = 0, \end{aligned} \tag{9}$$

where $Q_K = \delta_K / |\vec{v}_h|$ represents the stabilization coefficient associated with element K, δ_K being a suitable coefficient proportional to the element dimension (we refer to

Sect. 3.1 for an explicit expression of δ_K). Notice that the dispersion tensor $\vec{D}$ and the advective field $\vec{v}$ in (8) are here replaced by the discrete counterparts $\vec{D}_h$ and $\vec{v}_h$, respectively. In particular, the discrete tensor $\vec{D}_h$ is computed via (2) after substituting $\vec{v}$ with $\vec{v}_h$. Moreover, the meshes employed to discretize (6) and (9) may differ. In such a case, $\vec{v}_h$ will be projected on the $\mathbb{P}_1$ degrees of freedom.

Finally, the full discretization of problem (8) is obtained by discretizing the time dependence in (9) via the standard θ-method. For this purpose, we introduce a partition of the time window [0,T] by fixing the time levels $\{t^0,\dots,t^n\}$, with $t^0 \equiv 0$ and $t^n \equiv T$, which identify the set $\{I_k\}_{k=0}^{n-1}$ of the time intervals I_k of width $\Delta t^k = t^{k+1} - t^k$, for $k = 0,\dots,n-1$. To guarantee the unconditionally absolute stability of the θ-method, we set θ equal to $2/3$. This choice relieves us from any constraint in the choice of the time step in order to avoid the occurrence of spurious oscillations in the discrete solution. This is a crucial issue in view of the time adaptivity procedure in Sect. 4.2.

3 A Space-Time Recovery-Based Error Estimator

In this section, we provide the theoretical tools used to drive the space-time adaptive procedure. In particular, after introducing the framework used to settle the anisotropic mesh adaptivity, we furnish the *a posteriori* estimators for the control of the space and of the time discretization errors.

3.1 The Anisotropic Setting

Following the setting proposed in [21, 22], the anisotropic information is derived by introducing the standard invertible affine map $T_K : \widehat{K} \to K$ which transforms the equilateral triangle $\widehat{K}$ with vertices $(-\sqrt{3}/2,-1/2)$, $(\sqrt{3}/2,-1/2)$, $(0,1)$ into the generic triangle $K \in \mathscr{T}_h$. The triangle $\widehat{K}$ is inscribed in the unit circle centered at $(0,0)$. The map T_K changes this circle into an ellipse circumscribing K, as shown in Fig. 1. In particular, we have

$$\vec{x} = T_K\left(\widehat{\vec{x}}\right) = M_K\widehat{\vec{x}} + \vec{t}_K \quad \forall \vec{x} = (x_1,x_2)^T \in K,$$

with $\widehat{\vec{x}} = (\widehat{x}_1,\widehat{x}_2)^T \in \widehat{K}$, $M_K \in \mathbb{R}^{2\times 2}$ the Jacobian associated with the map T_K and $\vec{t}_K \in \mathbb{R}^2$ a shift vector. We exploit the spectral properties of M_K to describe the anisotropic features of the element K. To do this, first we introduce the polar decomposition $M_K = B_K Z_K$ of M_K, with $B_K \in \mathbb{R}^{2\times 2}$ a symmetric positive definite matrix and $Z_K \in \mathbb{R}^{2\times 2}$ an orthogonal matrix. Then, we consider the spectral decomposition $B_K = R_K^T \Lambda_K R_K$ of B_K, where $R_K^T = [\vec{r}_{1,K},\vec{r}_{2,K}] \in \mathbb{R}^{2\times 2}$ is the matrix of the right eigenvectors of B_K and $\Lambda_K = \mathrm{diag}\,(\lambda_{1,K},\lambda_{2,K})$ is the diagonal matrix of the corresponding eigenvalues, where we assume $\lambda_{1,K} \geq \lambda_{2,K}$.

Thus, shape, size and orientation of K are fully described by the quantities $\vec{r}_{i,K}$ and $\lambda_{i,K}$ for $i = 1,2$. In particular, $\vec{r}_{1,K}$ and $\vec{r}_{2,K}$ identify the directions of the two semi-axes of the ellipse circumscribing K, while $\lambda_{1,K}$ and $\lambda_{2,K}$ measure the length of these semi-axes

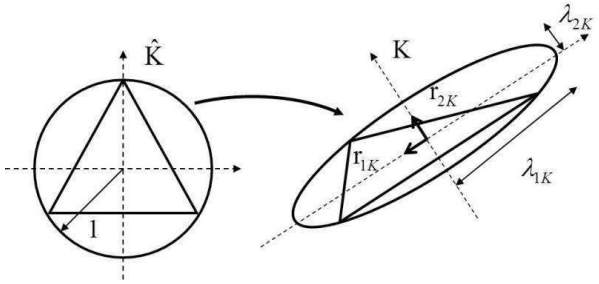

Figure 1: Geometric interpretation of the map T_K

(see Fig. 1). The aspect ratio $s_K = \lambda_{1,K}/\lambda_{2,K} \geq 1$ quantifies the deformation of triangle K. In particular, if K coincides with an equilateral triangle (the isotropic case), $s_K = 1$ while s_K increases as the shape of K stretches.

Now, we provide the anisotropic interpolation error estimate that inspired the estimator introduced in Sect. 3.2.1 for the spatial discretization error. Let I_h^1 be the Clément quasi-interpolant [14] defined, in the case of linear finite elements, by

$$I_h^1(u)(\mathbf{x}) = \sum_{N_j \in \mathscr{N}} P_j u(N_j)\, \varphi_j(\mathbf{x}) \quad \forall u \in L^2(\Omega),$$

where $\mathscr{N}$ is the set of the mesh vertices except the ones belonging to the Dirichlet portion Γ_1, φ_j is the Lagrangian basis function associated with the node N_j, and where $P_j u$ denotes the affine function associated with the patch Δ_j of the elements sharing node N_j defined by the relations

$$\int_{\Delta_j} \left(P_j u - u\right) \vartheta \, d\Delta_j = 0 \quad \text{with } \vartheta = 1, x_1, x_2.$$

The local feature of the employed error estimator leads us to introduce the restriction I_K^1 of I_h^1 to K, such that $I_K^1(u\big|_K) = I_h^1(u)\big|_K$ for any $u \in L^2(\Omega)$ and for any $K \in \mathscr{T}_h$. Moving from [21], we can state the following result

Lemma 3.1 *Let $\Delta_K = \{T \in \mathscr{T}_h \,:\, T \cap K \neq \emptyset\}$ be the patch of elements sharing at least a vertex with K, $\Delta_{\widehat{K}} = T_K^{-1}(\Delta_K)$ be the reference patch obtained by mapping back the whole Δ_K via the map T_K and let $u \in H^1(\Omega)$. Then, if $card(\Delta_K) \leq \mathscr{M}$ and $diam(\Delta_{\widehat{K}}) \leq \mathscr{N}_\Delta$, there exists a constant $C = C(\mathscr{M}, \mathscr{N}_\Delta)$ such that*

$$\|u - I_K^1(u)\|_{L^2(K)} \leq C \left[\sum_{i=1}^{2} \lambda_{i,K}^2 \left(\mathbf{r}_{i,K}^T G_K(u) \mathbf{r}_{i,K} \right) \right]^{1/2}, \tag{10}$$

where $G_K(u) \in \mathbb{R}^{2\times 2}$ is the symmetric positive semi-definite matrix given by

$$G_K(u) = \sum_{T \in \Delta_K} \begin{bmatrix} \displaystyle\int_T \left(\frac{\partial u}{\partial x_1}\right)^2 dT & \displaystyle\int_T \frac{\partial u}{\partial x_1}\frac{\partial u}{\partial x_2}\, dT \\ \displaystyle\int_T \frac{\partial u}{\partial x_1}\frac{\partial u}{\partial x_2}\, dT & \displaystyle\int_T \left(\frac{\partial u}{\partial x_2}\right)^2 dT \end{bmatrix}. \tag{11}$$

We highlight the explicit dependence of estimate (10) on the quantities $\mathbf{r}_{i,K}$ and $\lambda_{i,K}$, $i = 1,2$, which allows us to characterize anisotropically the triangle K, i.e., to fix its size, shape and orientation. Moreover, the conditions on Δ_K and $\Delta_{\widehat{K}}$ just avoid too distorted patches in the reference framework without introducing any limit on the anisotropic features of the mesh (we refer to [40] for examples of acceptable and not acceptable patches). When $\lambda_{1,K} \simeq \lambda_{2,K} \simeq h_K$, we recover the standard isotropic result [14]

$$\|u - I_K^1(u)\|_{L^2(K)} \leq C\, h_K\, |u|_{H^1(\Delta_K)}. \tag{12}$$

Note that the diameter h_K in (12) is replaced by the lenghts $\lambda_{i,K}$ in (10), while the components of the H^1-seminorm $|u|_{H^1}(\Delta_K)$ are projected along the anisotropic directions $\mathbf{r}_{i,K}$ via the terms $\mathbf{r}_{i,K}^T G_K(u)\mathbf{r}_{i,K}$.

Finally, we exploit the anisotropic spacing to fix the coefficient δ_K characterizing the stabilization coefficient Q_K in (9). Following [40], we set $\delta_K = \lambda_{2,K}/2$.

3.2 Recovery-Based Error Estimators

Recovery-based error estimators have been originally proposed by O.C. Zienkiewicz and J.Z. Zhu in the framework of linear elasticity [56, 57, 58]. The key idea underlying this class of error estimators is to improve the accuracy of the gradient of a numerical solution through suitable interpolation or averaging techniques, generally known as gradient recovery procedures. In a displacement-based finite element approach, the demand for a sharper numerical gradient arises from the necessity to deal with derived fields (e.g., stresses or strain rates) at least as accurate as the primary ones (e.g., displacements), due to their significant physical meaning in practical applications.

As a byproduct of the gradient recovery procedure, in [58] O.C. Zienkiewicz and J.Z. Zhu propose an *a posteriori* error estimator for the H^1-seminorm of the discretization error, simply defined as the L^2-norm of the difference between the recovered and the numerical gradient. This estimator is usually referred to as recovery-based. Many good properties characterize the recovery-based error estimators: they depend only on the adopted discrete space, being completely independent of the considered problem, of the governing equations and of the other details characterizing the adopted discrete formulation (e.g., the stabilization scheme); they are robust, easy to implement and cheap in terms of computational cost, since their definition involves only the numerical solution and the corresponding gradient. These properties make recovery-based error estimators a practical tool in view of an adaptive procedure and justify the extensive employment of these estimators in diverse applicative fields (see, e.g., [5, 33, 8, 43, 28]). More recently, an anisotropic version of the recovery-based error estimators has been proposed in [41] and successfully employed in two-dimensional as well as in three-dimensional settings [18, 39, 47, 46]. This anisotropic generalization allows us to combine the good properties of a recovery-based estimator with the richness of information needed for an anisotropic error analysis.

A theoretical investigation of the recovery-based error estimators is a recurrent but not yet very well understood issue in the literature, even in the simplest isotropic case [31, 42, 53, 10].

Following [47], in this section we resort to a recovery-based error estimator to adapt both the spatial mesh and the time step. For this purpose, we introduce an estimator η_{ht}^A to control the global (i.e., in space and time) discretization error where the space and time contributions are separate (see also [11, 37, 38, 50]), namely, such that

$$\eta_{ht}^A = \eta_h^A + \eta_t, \tag{13}$$

with η_h^A and η_t the space and time recovery-based error estimator, respectively. In particular, our interest in anisotropic adapted meshes leads us to identify η_h^A with an anisotropic error estimator. Estimators η_h^A and η_t are formulated separately in the two next sections.

3.2.1 The Spatial Error Estimator

Let us consider a generic time-dependent scalar variable z and let z_h be the corresponding linear finite element approximation. For any $t > 0$, we aim at providing an anisotropic estimate for the H^1-seminorm $\left|e_h^z(t)\right|_{H^1(\Omega)}^2 = \int_\Omega |\nabla z(t) - \nabla z_h(t)|^2 \, d\Omega$ of the discretization error $e_h^z(t) = z(t) - z_h(t)$. In an isotropic framework, the idea is to compute $e_h^z(t)$ by replacing the (generally) unknown exact gradient $\nabla z(t)$ with a suitable recovered gradient $P(\nabla z_h(t))$ [56, 57, 58], so that

$$\left|e_h^z(t)\right|_{H^1(\Omega)}^2 \simeq \int_\Omega |P(\nabla z_h(t)) - \nabla z_h(t)|^2 \, d\Omega = \left[\eta^{ZZ}(e_h^z(t))\right]^2. \tag{14}$$

To provide an anisotropic variant of estimator $\eta^{ZZ}(e_h^z(t))$, we refer to the anisotropic interpolation error estimate (10). In practice, by comparing estimates (10) and (12) we observe that the matrix $G_K(u)$ provides the anisotropic counterpart of the standard isotropic H^1-seminorm of u. This equivalence can be exploited for the definition of an anisotropic recovery-based error estimator, since $\eta^{ZZ}(e_h^z(t))$ in (14) coincides exactly with the H^1-seminorm of the *recovered error* $E(z_h(t)) = P(\nabla z_h(t)) - \nabla z_h(t)$. Thus, following [41, 18] and moving from definitions (10) and (14) we identify the spatial recovery-based anisotropic estimator to be replaced in (13) with

$$\left[\eta_h^A(e_h^z(t))\right]^2 = \sum_{K \in \mathscr{T}_h} \left[\eta_{K,h}^A(z_h(t))\right]^2, \tag{15}$$

where

$$\left[\eta_{K,h}^A(z_h(t))\right]^2 = \frac{1}{\lambda_{1,K}\lambda_{2,K}} \sum_{i=1}^{2} \lambda_{i,K}^2 \left(\mathbf{r}_{i,K}^T G_K(E_K(z_h(t))\mathbf{r}_{i,K}\right) \tag{16}$$

denotes the local error estimator, with $E_K(z_h(t)) = E(z_h(t))\big|_K$. The scaling factor $(\lambda_{1,K}\lambda_{2,K})^{-1}$ ensures the consistency with respect to the isotropic case, i.e., when we choose $\lambda_{1,K} = \lambda_{2,K}$, we get the isotropic estimator

$$\left[\eta_h^I(e_h^z(t))\right]^2 = \sum_{K \in \mathscr{T}_h} \left[\eta_{K,h}^I(z_h(t))\right]^2 \quad \text{with } \left[\eta_{K,h}^I(z_h(t))\right]^2 = \int_{\Delta_K} |(E_K(z_h(t))|^2 \, d\Delta_K.$$

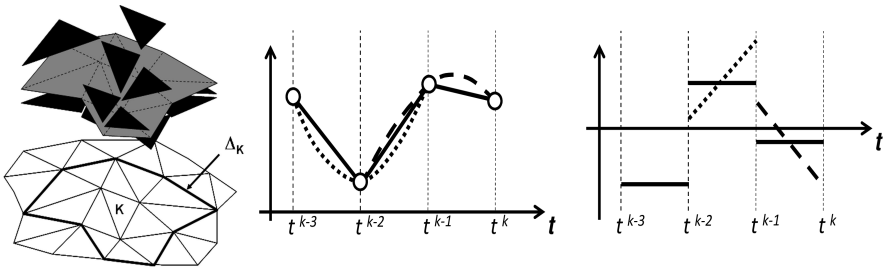

Figure 2: Spatial gradient recovery procedure (left): gradient of the discrete solution (black) and recovered gradient (grey); time gradient recovery (center): recovered solution z^R (dotted and dashed lines) and linear interpolant of values z_h^j (continuous line); time derivatives (right): $\partial z^R/\partial t$ (dotted and dashed lines), $\partial z_h/\partial t$ (continuous line)

Finally, the quantity z_h involved in (15) strictly depends on the problem at hand and identifies the physical quantity used to drive the spatial mesh adaptivity. Estimator (15) may be applied to more general problems involving not only scalar quantities, such as the elasticity or the Navier-Stokes equations [18].

We detail in the following the adopted gradient recovery procedure. Several recipes have been provided in the literature to compute the recovered gradient (see, e.g., [57, 48, 10, 33]). Following [41], we resort here to a very simple approach which defines a patchwise constant recovered gradient. We let

$$P_{\Delta_K}(\nabla z_h)(\vec{x},t) = \frac{1}{|\Delta_K|}\sum_{T\in\Delta_K}|T|\,\nabla z_h(t)\big|_T \quad \text{with } \vec{x}\in K,\ t>0, \tag{17}$$

with $|\varpi|$ the measure of the generic set $\varpi \subset \mathbb{R}^2$, namely we compute the area-weighted average over the whole patch Δ_K of the gradients of the discrete solution and then we assign such a value to the single element K (see Fig. 2, left for a sketch of the recovery procedure). Thus, for any element $K' \in \Delta_K$ with $K' \neq K$, $P_{\Delta_{K'}}(\nabla z_h)$ is, in general, different from $P_{\Delta_K}(\nabla z_h)$, and it is constant on the patch $\Delta_{K'}$. In view of a practical implementation, the time t in (17) coincides with a time level t^k of the time partition $\{t^0,\ldots,t^n\}$. The recovery procedure in (17) can be generalized to higher degree polynomials as shown in [41]. Here, to contain the computational costs, we adopt the simplest choice, i.e., z_h coincides with a piecewise linear function.

Despite the heuristic nature of the anisotropic estimator $\eta_h^A(e_h^z(t))$, a corresponding theoretical background is furnished in [41], where a patch test on the estimator is provided and an equivalence relation between the local estimator $\eta_{K,h}^A(z_h(t))$ and the H^1-seminorm of the discretization error on the patch Δ_K is derived.

Finally, estimator $\eta_h^A(e_h^z(t))$ has been successfully extended and assessed in a three-dimensional setting in [18, 39].

3.2.2 The Time Error Estimator

The actual goal pursued in our time adaptive procedure is to predict, at the generic time level t^k, the time step Δt^k identifying interval I_k. Following [47], this prediction is carried out by defining a local time error estimator instead of the global one η_t in (13). As a consequence, we observe that the number n of time intervals is not known *a priori* but it will be fixed by the adaptive procedure itself. As in Sect. 3.2.1, we consider a generic scalar variable z together with the corresponding linear finite element approximation z_h. Then, in the spirit of a recovery-based error estimator, we move from the H^1-seminorm of the time discretization error on the time interval I_{k-1}

$$\left|e_h^z(\vec{x})\right|^2_{H^1(I_{k-1})} = \int_{I_{k-1}} \left| \frac{\partial z(\vec{x})}{\partial t} - \frac{\partial z_h(\vec{x})}{\partial t} \right|^2 dt. \tag{18}$$

Of course, at the generic time level t^k, we know z_h at all the previous times t^i, with $i = 0, \ldots, k-1$. Now, the idea is to replace the two time derivatives in (18) with two easily computable quantities. We approximate the derivative of the discrete solution, $\partial z_h(\vec{x})/\partial t$, by replacing z_h with the straight line interpolating z_h at t^{k-1} and t^k (see Fig. 2, center), so that

$$\frac{\partial z_h(\vec{x})}{\partial t}\Big|_{I_{k-1}} \simeq \frac{z_h^k - z_h^{k-1}}{\Delta t^{k-1}},$$

with $z_h^j = z_h(\vec{x}, t^j)$ for $j = 0, \ldots, n$. To replace $\partial z(\vec{x})/\partial t$, we first substitute z with a suitable recovered solution z^R and then we compute $\partial z(\vec{x})/\partial t$ as $\partial z^R(\vec{x})/\partial t$. In particular, we select z^R as the parabola interpolating the pairs of values (t^{k-2}, z_h^{k-2}), (t^{k-1}, z_h^{k-1}), (t^k, z_h^k) (see Fig. 2, center). Notice that this choice leads to a piecewise linear recovered gradient in contrast to the piecewise constant discrete quantity $\partial z_h(\vec{x})/\partial t$ (see Fig. 2, right), in agreement with a standard recovery-based approach. Thus, the H^1-seminorm in (18) is approximated via the local time recovery-based error estimator $\eta_{k-1,t}(z_h(\vec{x}))$ as

$$\left|e_h^z(\vec{x})\right|^2_{H^1(I_{k-1})} \simeq \widetilde{T} \int_{I_{k-1}} \left| \frac{\partial z^R(\vec{x})}{\partial t}\Big|_{I_{k-1}} - \frac{z_h^k - z_h^{k-1}}{\Delta t^{k-1}} \right|^2 dt = \left[\eta_{k-1,t}(z_h(\vec{x}))\right]^2, \tag{19}$$

with $\widetilde{T}$ a suitable time scale factor typical of the problem at hand. Different choices are possible for $\widetilde{T}$. It may just coincide with the time step Δt^{k-1} or it may be related to geometrical and/or physical quantities, e.g., we can choose $\widetilde{T} = L/w$, with L a characteristic length of the domain Ω and w a representative velocity. In the numerical validation of Sect. 5, we always choose $\widetilde{T} = \Delta t^{k-1}$. Factor $\widetilde{T}$ essentially makes the time estimator dimensionless, i.e., suited to be added to the dimensionless space estimator $\eta_h^A(e_h^z(t))$ in view of (13). Estimator $\eta_{k-1,t}(z_h(\vec{x}))$ can be evaluated at each vertex N of the mesh, i.e., for any $\vec{x} \equiv N$. Nevertheless, we need in practice a unique value for such an estimator on the interval I_{k-1}. With this aim, we first obtain a unique value on the generic triangle $K \in \mathcal{T}_h$ simply by considering the mean of the values at the three vertices of K

$$\left[\eta_{k-1,t,K}(z_h)\right]^2 = \frac{1}{3} \sum_{N \in K} \left[\eta_{k-1,t}(z_h(N))\right]^2.$$

Then, we lump the information on the whole mesh by introducing the further area-weighted average

$$\left[\eta_{k-1,t}(z_h)\right]^2 = \frac{1}{\sum\limits_{K\in\mathscr{T}_h}|K|}\sum_{K\in\mathscr{T}_h}|K|\left[\eta_{k-1,t,K}(z_h)\right]^2. \tag{20}$$

In [47] we employ a standard sum over the mesh elements to get the value $\eta_{k-1,t}(z_h)$. The variant in (20) normalizes the time error estimator with respect to the domain dimension. This makes the element time estimators comparable even in the presence of strongly non-uniform spatial meshes. Finally, in view of the time adaptive procedure in the next section, we formally introduce the global time error estimator

$$\left[\eta_t(e_h^z)\right]^2 = \sum_{k=1}^{n}\left[\eta_{k-1,t}(z_h)\right]^2 \tag{21}$$

which can be introduced in (13). Notice that the number n of time subintervals involved in (21) represents an unknown of the space-time adaptive procedure.

4 The Solution-Adaptation Procedure

We illustrate here how we combine the discretization of ADE (1) with the information provided by the error estimators $\eta_h^A(e_h^z(t))$ and $\eta_t(e_h^z(\vec{x}))$ to automatically adapt the spatial mesh $\mathscr{T}_h$ and the discretization of the time window $[0,T]$ to model an unsteady solute transport process. We aim at guaranteeing the total error below a certain global tolerance τ. Following [38], we split this tolerance by setting a space and a time tolerance, τ_h and τ_t, respectively such that $\tau = \tau_h + \tau_t$. Tolerance τ_h will drive the mesh adaptive procedure detailed in Sect. 4.1, while τ_t will lead us to identify the next time step via the predictive procedure in Sect. 4.2. The algorithm coupling these two adaptive procedures with the discrete solver for (1) is then provided in Sect. 4.3.

4.1 Spatial Mesh Adaptivity

We resort to a well-established metric-based adaptive procedure, following the approach proposed in [22] and successfully employed in a number of works (see, e.g., [38, 41, 46, 18]). In particular, the adapted mesh is built starting from a metric induced by the error estimator $\eta_h^A(e_h^z(t))$ so that the number of mesh elements is minimized and the tolerance τ_h is guaranteed on $\eta_h^A(e_h^z(t))$ via an error equidistribution criterion.

According to the generic definition, a metric is a symmetric positive definite tensor field $\mathscr{M} : \Omega \to \mathbb{R}^{2\times 2}$, such that $\mathscr{M}(\vec{x}) = \widetilde{R}^T(\vec{x})\widetilde{\Lambda}^{-2}(\vec{x})\widetilde{R}(\vec{x})$ for any $\vec{x}\in\Omega$, with $\widetilde{\Lambda}(\vec{x}) = \mathrm{diag}(\widetilde{\lambda}_1(\vec{x}),\widetilde{\lambda}_2(\vec{x}))$ and $\widetilde{R}^T(\vec{x}) = [\widetilde{\vec{r}}_1(\vec{x}),\widetilde{\vec{r}}_2(\vec{x})]$ a positive diagonal and an orthogonal tensor, respectively [24]. For an assigned mesh $\mathscr{T}_h$, it is a standard practice to approximate the pointwise tensors $\widetilde{\Lambda}(\vec{x})$ and $\widetilde{R}(\vec{x})$ via quantities which are piecewise constant on $\mathscr{T}_h$, so that $\widetilde{\lambda}_i(\vec{x})\big|_K = \widetilde{\lambda}_{i,K}$, $\widetilde{\vec{r}}_i(\vec{x})\big|_K = \widetilde{\vec{r}}_{i,K}$ for any $K\in\mathscr{T}_h$ and for $i = 1,2$.

Now, we briefly explain how to associate a piecewise constant metric $\mathscr{M}_\eta$ with a background grid $\mathscr{T}_h^B$ by exploiting the anisotropic spatial error estimator in (15)-(16) evaluated on $\mathscr{T}_h^B$. For the sake of simplicity, we drop the time dependence in (15)-(16). In particular, we focus on the local estimator $\eta_{K,h}^A(z_h)$. We properly rewrite it, by collecting the area information in a unique multiplicative factor, i.e., as

$$\left[\eta_{K,h}^A(z_h)\right]^2 = |\Delta_{\widehat{K}}|\,\lambda_{1,K}\lambda_{2,K}\left\{s_K\left(\mathbf{r}_{1,K}^T G_K^*(E_K(z_h))\mathbf{r}_{1,K}\right) + s_K^{-1}\left(\mathbf{r}_{2,K}^T G_K^*(E_K(z_h))\mathbf{r}_{2,K}\right)\right\} \tag{22}$$

where $G_K^*(E_K(z_h)) = G_K(E_K(z_h))/|\Delta_K|$, with $|\Delta_K| = |\Delta_{\widehat{K}}|\,\lambda_{1,K}\lambda_{2,K}$ and $\Delta_{\widehat{K}}$ defined as in Lemma 3.1. Now, the idea is to apply an error equidistribution criterion to guarantee that each element $K \in \mathscr{T}_h^B$ provides the same contribution to the global error, i.e., to ensure that $\left[\eta_{K,h}^A(z_h)\right]^2 = \tau_{loc}^2$, where $\tau_{loc} = \tau_h/\text{card}(\mathscr{T}_h^B)$ is the local tolerance, with $\text{card}(\mathscr{T}_h^B)$ the cardinality of the background grid. At the same time, we aim at minimizing the number of mesh elements, which is equivalent to maximizing the area of each triangle K. Consequently, we minimize the term in brackets in (22), i.e., for each $K \in \mathscr{T}_h^B$, we solve the minimization problem

$$\text{find } \{s_K, \mathbf{r}_{1,K}\} \;:\; s_K\left(\mathbf{r}_{1,K}^T G_K^*(E_K(z_h))\mathbf{r}_{1,K}\right) + s_K^{-1}\left(\mathbf{r}_{2,K}^T G_K^*(E_K(z_h))\mathbf{r}_{2,K} \text{ is minimum,}\right.$$

constrained by the following requirements $s_K \geq 1$, $\|\mathbf{r}_{1,K}\|_2 = \|\mathbf{r}_{2,K}\|_2 = 1$, $\mathbf{r}_{1,K}\cdot\mathbf{r}_{2,K} = 0$. As shown in [42], there exists a unique analytical solution to this problem which provides the *optimal* aspect ratio $\widetilde{s}_K^\eta = \sqrt{\gamma_{1,K}/\gamma_{2,K}}$ and the *optimal* direction $\widetilde{\mathbf{r}}_{1,K}^\eta = \mathbf{g}_{2,K}$, with $\gamma_{1,K} \geq \gamma_{2,K}$ the eigenvalues of $G_K^*(E_K(z_h))$ and $\mathbf{g}_{2,K}$ the eigenvector associated with $\gamma_{2,K}$. The metric $\mathscr{M}_\eta$ is then completely identified by deriving two separate *optimal* values $\widetilde{\lambda}_{1,K}^\eta$, $\widetilde{\lambda}_{2,K}^\eta$ from $\widetilde{s}_K^\eta$. With this aim, we exploit the error equidistribution to get $\widetilde{\lambda}_{1,K}^\eta = \sqrt{p\,\widetilde{s}_K^\eta}$, $\widetilde{\lambda}_{2,K}^\eta = \sqrt{p/\widetilde{s}_K^\eta}$, with

$$p = \widetilde{\lambda}_{1,K}^\eta\,\widetilde{\lambda}_{2,K}^\eta = \tau_{loc}^2\left[|\Delta_{\widehat{K}}|\,(\widetilde{s}_K^\eta\,\gamma_{2,K} + (\widetilde{s}_K^\eta)^{-1}\,\gamma_{1,K})\right]^{-1}. \tag{23}$$

To summarize, the metric $\mathscr{M}^\eta$ induced by $\eta_h^A(e_h^z(t))$ is univocally identified by the triplets $\left\{\widetilde{\lambda}_{1,K}^\eta, \widetilde{\lambda}_{2,K}^\eta, \widetilde{\mathbf{r}}_{1,K}^\eta\right\}$, with $K \in \mathscr{T}_h^B$. This provides us with an *optimal* metric, which minimizes the number of elements, while guaranteeing the desired global accuracy τ_h and the equidistribution of the spatial discretization error.

Finally, the new adapted mesh is generated moving from the metric $\mathscr{M}^\eta$ and the background grid $\mathscr{T}_h^B$. To this end, we employ the two-dimensional metric-based mesh generator BAMG which performs a remesh on $\mathscr{T}_h^B$, although trying to preserve the original position of the mesh nodes [27].

The generation of the adapted mesh is constrained by some additional checks. In particular, we avoid an excessive element clustering, for instance where solution discontinuities occur, by setting a minimum value p_{min} on the product $\widetilde{\lambda}_{1,K}^\eta\,\widetilde{\lambda}_{2,K}^\eta$, i.e., on the minimum area allowed for K. In practice, we predict p via (23) and then we set $p = \max(p, p_{min})$. We also check the number of the triangles predicted by the metric $\mathscr{M}^\eta$. We impose that the cardinality of the adapted mesh belongs to a specific interval

$[\mathcal{N}_{min}, \mathcal{N}_{max}]$, to prevent an extreme coarsening or refinement of the mesh elements. In particular, we predict the number of elements associated with the metric $\mathcal{M}^{\eta}$; if this number is smaller than $\mathcal{N}_{min}$ or greater than $\mathcal{N}_{max}$, we generate a new metric via a global and uniform scaling of the tensor $\mathcal{M}^{\eta}$. This check turns out to be crucial especially in the presence of unsteady phenomena characterized by a strong heterogeneity of space-time dynamics.

4.2 Time Step Adaptivity

Goal of the time step adaptivity here proposed is to predict, at each time t^k, the time step Δt^k which identifies the next time level t^{k+1}. An error equidistribution criterion is pursued also in this case. Nevertheless, since the total number of time intervals is determined only at the end of the adaptive procedure, we fix a local tolerance $\tau_t^{\Delta t}$ to be associated with each I_k instead of the global tolerance τ_t as in (13). Following [47], we rewrite the time error estimator in (20) as

$$\left[\eta_{k-1,t}(z_h)\right]^2 = \left[\Delta t^{k-1}\rho_{k-1,t}(z_h)\right]^2 \tag{24}$$

with

$$\left[\rho_{k-1,t}(z_h)\right]^2 = \frac{1}{\left[\Delta t^{k-1}\right]^2 \sum_{K\in\mathcal{T}_h^k} |K|} \sum_{K\in\mathcal{T}_h^k} |K| \left[\eta_{k-1,t,K}(z_h)\right]^2$$

and where $\mathcal{T}_h^k$ denotes the spatial mesh associated with the time t^k. Relation (24) is now exploited to predict Δt^k. In particular, after imposing $\eta_{k-1,t}(z_h) = \tau_t^{\Delta t}$, we solve (24) with respect to the time step and we obtain

$$\Delta t^k = \frac{\tau_t^{\Delta t}}{\rho_{k-1,t}(z_h)}. \tag{25}$$

Finally, we check that the time step predicted in (25) belongs to a suitable range of variation $[\Delta t_{min}, \Delta t_{max}]$, fixed *a priori* according to the temporal scales involved in the problem at hand. This control improves the global stability and accuracy of the whole adaptive procedure. Finally, since the time recovery procedure (19) involves the three times t^k, t^{k-1}, t^{k-2}, we are obliged to assign *a priori* the time steps Δt^0 and Δt^1, which are both set to Δt_{min} in the numerical validation below.

4.3 Coupling Discretization with Adaptivity

We detail here the strategy followed to combine the discretization in Sect. 2.1 with the space and time adaptive procedures of Sect. 4.1-4.2, in view of a reliable and efficient modeling of unsteady solute transport processes. For this purpose, we identify the scalar variable z driving the adaptive procedure with the concentration C.

To start the solution-adaptation procedure, we have to preliminarily assign the initial datum C_0 in (3) as well as the velocity field $\vec{v}$, solution to Darcy's problem (4), on a sufficiently fine initial grid $\mathcal{T}_h^0$. We focus now on the generic time t^{k-1}, i.e., we

assume to know the discrete concentration field $C_h^{k-1} = C_h(t^{k-1})$ at time t^{k-1}, the mesh $\mathcal{T}_h^{k-1}$ and the time step Δ^{k-1}, both predicted at the previous time step. First of all, we discretize equation (1) on the interval I_{k-1} via the stabilized finite element scheme (9), thus yielding the approximate solution C_h^{*k} at time t^k. This solution is employed to generate the next adapted mesh, $\mathcal{T}_h^k$, following the anisotropic adaptive procedure detailed in Sect. 4.1, after identifying z_h with C_h^{*k} and $\mathcal{T}_h^B$ with $\mathcal{T}_h^{k-1}$. Then, all the quantities associated with $\mathcal{T}_h^{k-1}$ are projected on the new mesh $\mathcal{T}_h^k$. This last projection leads us to define the actual value, C_h^k, of the concentration field at the time t^k. Notice that, to contain the computational cost characterizing the whole time window, we do not resort to an iterative procedure to get the adapted mesh $\mathcal{T}_h^k$, by demanding, for instance, a stagnation of the number of mesh elements (see, e.g., [38]). On the contrary, the mesh identified by the optimal metric in Sect. 4.1 is directly assumed as the mesh to be associated with time t^k. Finally, moving from the approximate solutions C_h^k, C_h^{k-1} and C_h^{k-2}, we predict the next time step Δt^k (i.e., the new time level t^{k+1}) via the time adaptive procedure in Sect. 4.2, after setting $z_h = C_h$ and a local time tolerance $\tau_t^{\Delta t}$. The whole procedure is sketched in Fig. 3.

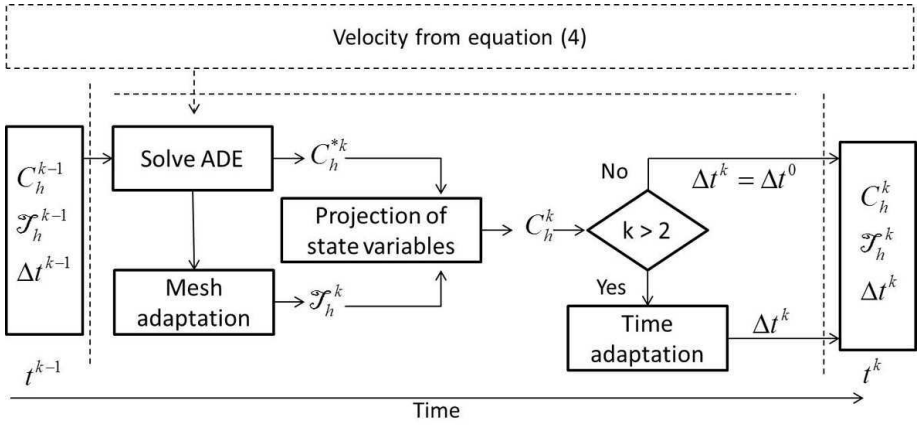

Figure 3: Sketch of the solution-adaptation procedure

Concerning the projection step, following [47], we resort to a standard L^2-projection which exhibits good conservation properties when applied, for instance, to the unsteady shallow water equations [46]. More sophisticated recipes to deal with such a projection are available in the literature (see, e.g., [1, 19]).

5 Numerical Results

We assess here the methodology introduced in Sect. 3-4. In particular, we first perform a quantitative investigation by considering a test case characterized by an analytical solution. Then, we model a solute transport experiment performed in a homogeneous sand box. For this test case, a comparison with experimental measurements is provided as well.

5.1 Analytical Test Case

We consider a two-dimensional solute transport problem assigned in the semi-infinite rectangular domain $\Omega = (0,+\infty)\times(0,W)$[m]. A constant solute concentration $C_{in} = 1$ is introduced into the domain at the inlet section Γ_{in} corresponding to the segment $\{(x_1,x_2) \ : \ x_1 = 0\text{m}, x_2 \in [Y_1,Y_2]\text{m}\}$. A zero-flux boundary condition is imposed on the remaining part of the left-side boundary as well as on the top and bottom edges. Then, we assume that a horizontal uniform velocity field $\vec{v} = (v_1,0)^T$, with $v_1 \geq 0$, is applied to the system, while we choose $D_m = 0$, $\alpha_L = 0.1$m and $\alpha_T = 0.05$m in (2) and the initial value $C_0 = 0$. An implicit analytical expression for the concentration field C, solution to (1), is available in [52] and coincides with

$$C(x_1,x_2,t) = \sum_{n=0}^{+\infty} L_n P_n \cos(\eta x_2) \quad \left\{ \exp\left[\frac{x_1(v_1-\beta)}{2D_{11}}\right] \text{erfc}\left[\frac{x_1-\beta t}{2\sqrt{D_{11}t}}\right] + \exp\left[\frac{x_1(v_1+\beta)}{2D_{11}}\right] \text{erfc}\left[\frac{x_1+\beta t}{2\sqrt{D_{11}t}}\right] \right\}, \tag{26}$$

with

$$L_n = \begin{cases} \frac{1}{2} & \text{if } n = 0 \\ 1 & \text{if } n > 0, \end{cases} \qquad P_n = \begin{cases} \dfrac{Y_2 - Y_1}{W} & \text{if } n = 0 \\ \dfrac{[\sin(\eta Y_2) - \sin(\eta Y_1)]}{n\pi} & \text{if } n > 0, \end{cases}$$

$$\eta = n\pi/W, \qquad \beta = \sqrt{v_1^2 + 4D_{11}(\eta^2 D_{22})},$$

where erfc is the complementary error function, while D_{11}, D_{22} denote the diagonal components of the dispersion tensor $\mathbf{D}$ according to (2). In particular, we set $Y_1 = 0.13$m, $Y_2 = 0.67$m, $W = 1$m and $v_1 = 10^{-3}$m/s. These values, together with the choices made for α_T and α_L, are representative of a typical laboratory scale transport setting.

The analytical solution (26) allows us to investigate the convergence properties of the proposed adaptive procedure. We perform this analysis for a fixed time level $t^* = 150$s, when the solute concentration C already exhibits a moderate spread within the domain as shown in Fig. 4-a). Figure 4-b) shows the corresponding anisotropic adapted mesh. The anisotropic features of the solution are not so marked. This is confirmed by the corresponding maximum value of the aspect ratio which is about equal to 8. We analyze the trend of the $H^1(\Omega)$-seminorm of the spatial discretization error $e_h^C(t^*) = C(t^*) - C_h(t^*)$ at time t^*. Concerning the evaluation of the exact solution, we truncate the series (26) at the hundredth term while, to mimic the semi-infinite domain, we identify Ω with a rectangular domain whose right side is sufficiently far from the left one so that it is never reached by the phenomenon at hand. Homogeneous Neumann condition are assigned along this fictitious boundary. In Fig. 4-c) we compare the trend of the error $e_h^C(t^*)$ as a function of the number of elements. We consider three different space-time discretization strategies: i) fixed and uniform space-time grids; ii) meshes anisotropically adapted in space, but fixed and uniform in time; iii) meshes adapted both in space and time, with an anisotropic adaptivity in space. The slope of the three curves is comparable and consistent with the expected order of convergence, i.e., $-1/2$,

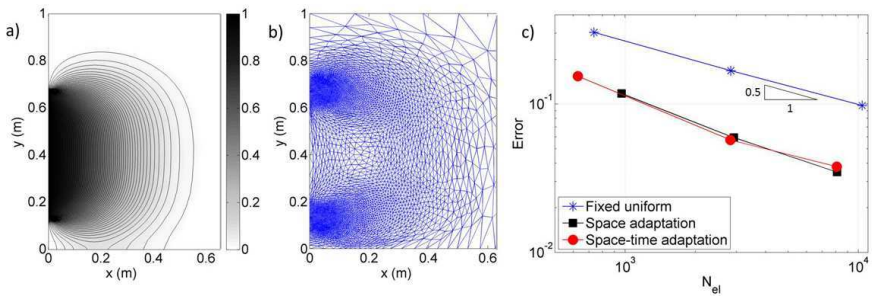

Figure 4: Analytical test case: a) contour plot of the concentration field in (26) for $t^* = 150$s; b) corresponding anisotropic adapted mesh; c) trend of the $H^1(\Omega)$-seminorm of the relative error for different space-time meshes

Table 1: Analytical test case: quantitative information associated with the convergence analysis

	Fixed uniform			Space adaptivity			Space-time adaptivity		
N_{el}	732	2482	10388	967	2928	8104	627	2829	8081
$N_{\Delta t}$	150	150	150	150	150	150	54	36	32
$\left\|e_h^C(t^*)\right\|_{H^1}$	$3\cdot10^{-1}$	$1.70\cdot10^{-1}$	$9.7\cdot10^{-2}$	$1.18\cdot10^{-1}$	$5.93\cdot10^{-2}$	$3.47\cdot10^{-2}$	$1.54\cdot10^{-1}$	$5.72\cdot10^{-2}$	$3.78\cdot10^{-2}$

while it is evident that, for a given number of mesh elements, the error associated with the fixed space-time mesh is the largest one.

More quantitative information are provided in Table 1. For each type of mesh, we furnish the mesh cardinality, $\#\mathcal{T}_h$, the number, $\mathcal{N}_{\Delta t}$, of time steps used to reach time t^* and the $H^1(\Omega)$-seminorm of the error $e_h^C(t^*)$. Of course, a different tolerance τ_h and different values for $\mathcal{N}_{min}$ and $\mathcal{N}_{max}$ drive the mesh adaptive procedure through the columns of the table. The choice $p_{min} = 10^{-5}$ is common to all the simulations. The time step is set to $\Delta t = 1$s for the fixed uniform and space adaptive simulations (first two macro-columns in Table 1), while we set $\Delta t_{min} = 1$s and $\Delta t_{max} = 20$s for the space-time adaptive procedure (i.e., in the third macro-column in Table 1). An error of approximately 10% is obtained with a fixed space-time grid of approximately $10,000$ triangles and 150 time intervals. On the other hand, for the same $\mathcal{N}_{\Delta t}$, we are able to guarantee a better accuracy (i.e., an error of about 6%) via an anisotropic adapted mesh consisting of about $3,000$ triangles only. When also the time step is also adapted, we obtain a comparable error by resorting to a similar number of elements but reducing $\mathcal{N}_{\Delta t}$ by a factor four. A comparison between the second and the third macro-column shows that for a comparable number of mesh elements, the number of time intervals predicted by the time adaptive procedure is significantly reduced (i.e., by a factor comprised between three and five).

5.2 Solute Transport in a Homogeneous Sand Box

Goal of this section is to compare the results provided by our numerical approach with experimental data. This provides an important added value to this work. The experiments are performed within a square flow cell with an extension of $0.249 \times 0.249\text{m}^2$ and a thickness of 1.5cm. The inlet and outlet sections are located near the bottom-left and the top-right corner, respectively as shown in Fig. 5-a). The width of the inflow and outflow sections is very small, equal to 3mm. The flow cell is packed with a homogeneous sand with porosity $\phi = 0.325$ and permeability $k = 1.4256 \cdot 10^{-10}\text{m}^2$ while, since the fluid is simply water, we set the viscosity μ and density ρ to 10^{-3}Pa·s and $1,000\text{Kg/m}^3$, respectively [32]. The solute concentration in the system is zero at the beginning of the experiment. A solution containing a constant concentration C_{in} is then introduced as a step-input at the inlet, while a zero flux condition is imposed on the remaining part of $\partial\Omega$. The injection flow rate is constant in time and equal to $Q_{in} = 4\text{ml/s}$. The available experimental measurements correspond to the time evolution of the average concentration at the outflow section, i.e., they coincide with the breakthrough curve

$$C_{out}(t) = \frac{1}{|\Gamma_{out}|} \int_{\Gamma_{out}} C(\vec{x},t) d\Gamma \quad \forall t \in [0,T], \tag{27}$$

where Γ_{out} is the outflow section and $|\Gamma_{out}|$ denotes its length. We consider here data from two identical experimental tests to increase the robustness of the results with respect to measurement errors.

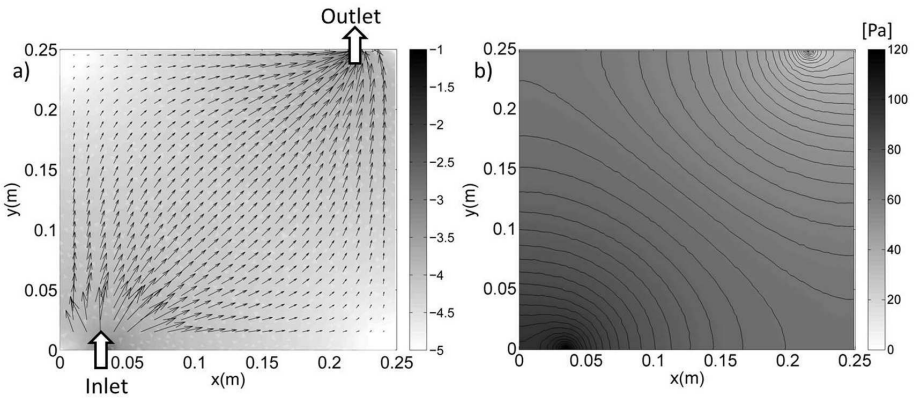

Figure 5: Experimental flow cell: a) velocity vector field superimposed to the color map of $\log_{10} \|\vec{v}\|_2$; b) pressure contour plot

The velocity field $\vec{v}$ is obtained by approximating (4) through the discrete formulation (7) on a fixed uniform unstructured grid of $22,108$ elements. Fig. 5 shows the pressure contour plot in panel b), and the velocity vector field superimposed to the contour plot of the corresponding modulus in logarithmic scale in panel a). A constant (atmospheric) pressure is imposed at the outlet boundary, while we set $\vec{v} \cdot \vec{n} = Q_{in}/A_{in}$

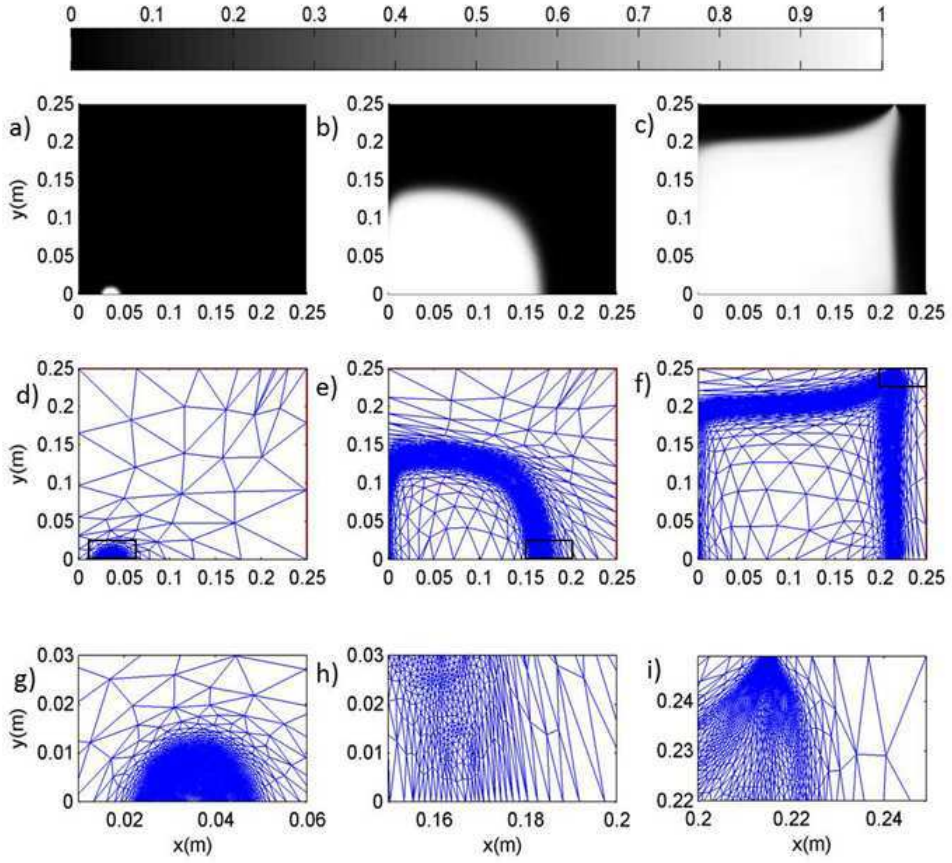

Figure 6: Experimental flow cell: solute concentration field a)-c); associated anisotropic adapted mesh d)-f); details of the adapted mesh g)-i) for $t = 10$s (left), $t = 1,500$s (center), $t = 3,000$s (right)

at the inlet, A_{in} being the area of the inflow cross section. The remaining parts of the boundary of the flow cell are considered as impermeable, i.e., we set $\vec{v} \cdot \vec{n} = 0$.
Then, the solute transport is modeled by means of the space-time adaptive procedure detailed in Sect. 4 within the time window $[0, 12,000]$s. The dispersivities α_L and α_T are set to 10^{-4}m and 10^{-5}m, respectively, upon preliminary visual calibration against experimental data. The effect of molecular diffusion is here embedded in the dispersion coefficients, i.e., we set $D_m = 0$. In the following, we describe the process evolution, we provide a comparison with experimental measurements and, finally, we discuss the sensitivity of the numerical results to the parameters involved in the space-time adaptive technique.
Figure 6-a)-c) shows some snapshots of the concentration evolution. During the first instants the solute spreads radially into the cell, around the inflow section (Fig. 6-a). Then,

the advective field and the dispersive processes deform and displace the concentration front towards the center of the cell (Fig. 6-b). At time $t \approx 3,000$s, the solute reaches the outlet boundary following a preferential flow path (Fig. 6-c). For longer times, the solute slowly spreads towards the top-left and bottom-right corners of the cell. At the final time $T = 12,000$s, the cell is characterized by a constant concentration equal to one. In Fig. 6-d)-f) we gather the corresponding anisotropic adapted meshes, while a zoom in on the boxed areas is provided in the last row of the figure. A good matching between solution and mesh can be observed. The refinement of the mesh essentially follows the advancing front, where the gradient variations are significant, while a general coarsening occurs where the concentration is basically uniform. The anisotropic features of the adapted mesh become more significant when the front develops and gradually spreads the cell (see the enlarged views in Fig. 6-h and 6-i). On the contrary, at the initial times the triangles are clustered around the inlet section but they exhibit a mild anisotropy, due to extremely reduced size of the concentration front. Thus, the maximum value of the aspect ratio increases in time, and corresponds to 26.5 to 27.8 until 49.82 for the meshes displayed in Fig. 6-d), -e), -f), respectively. The maximum value reached by s_K on the whole time window is 407.18. To obtain the results in Fig. 6, we have employed the following setting for the parameters involved in the space-time adaptive procedure: concerning the adaptivity in space we choose $\tau_h = 0.7$, $\mathcal{N}_{min} = 400$ and $\mathcal{N}_{max} = 10,000$ while the adaptivity in time is performed by assigning the values $\tau_t^{\Delta t} = 0.17$, $\Delta t_{min} = 1$s and $\Delta t_{max} = 50$s.

The numerical validation demonstrates that the value p_{min} proportional to the minimum allowed element area plays a critical role in the adaptive procedure. In principle, the choice $p_{min} = 10^{-6}\text{m}^2$ should allow to capture all the meaningful details of the process at hand since the whole flow cell area is equal to 0.062m^2. Nevertheless, this value is still too large to provide an accurate approximation of the solute behaviour at the outlet and inlet cross sections, which are 3mm wide. This represents a critical issue for two important reasons: (i) a sharp discretization of the concentration field at the inlet is crucial to capture the initial times of the solute evolution and, consequently, to allow the correct development of the phenomenon; (ii) a proper discretization of the concentration at the outlet is essential to compare the numerical results with the experimental measurements that we have at our disposal, i.e., with the breakthrough curve (27). To take into account both these demands, we introduce an adaptive choice of the quantity p_{min} during the simulation time window, following this two-value strategy: for $t < 20$s, we set $p_{min} = 10^{-9}\text{m}^2$ to properly model the solution near the inflow section (see Fig. 6-d and 6-g); in the next phase, we increase p_{min} to 10^{-6}m^2 to save computational resources (see Fig. 6-e and 6-h); then, as soon as we detect at the outlet concentration values above a given threshold (set to 10^{-3} in this application), we set again $p_{min} = 10^{-9}\text{m}^2$ (see Fig. 6-f and 6-i).

We deal now with the comparison between the numerically computed and experimentally measured breakthrough curves. As for the previous test case, we consider three different space-time discretization strategies, namely, a fixed uniform space-time mesh, a mesh anisotropically adapted in space but fixed and uniform in time, a fully adapted mesh, i.e., adapted both in space and time. The fixed uniform mesh is char-

acterized approximatively by $10,000$ elements, while the discretization step is $\Delta t = 1$s. When we adapt the spatial mesh only, we set $\tau_h = 0.7$ and preserve the constant time step $\Delta t = 1$[s]. Finally, the fully adaptive procedure is associated with the values $\tau_h = 0.7$ and $\tau_t^{\Delta t} = 0.14$.

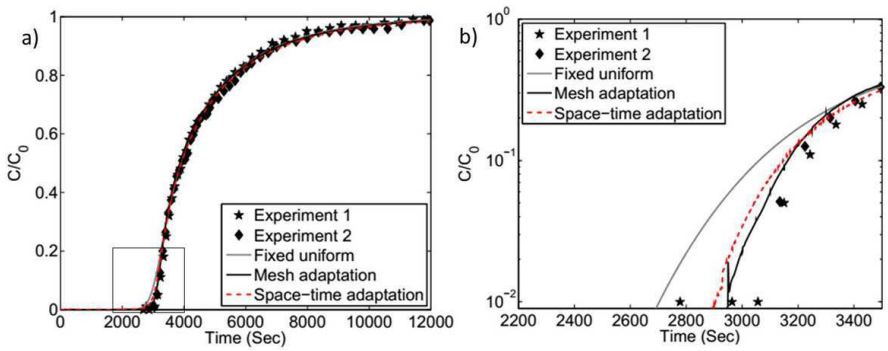

Figure 7: Experimental flow cell: a) comparison of experimental measurements with the numerical breakthrough curves for three different choices of the space-time mesh; b) enlarged view on the early solute breakthrough in semi-logarithmic scale

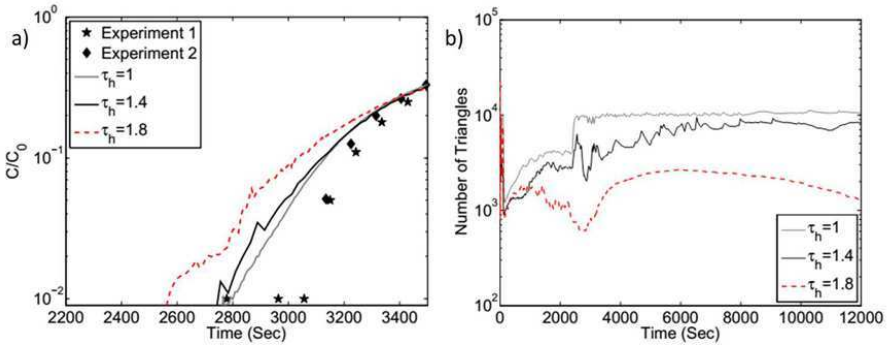

Figure 8: Experimental flow cell: a) comparison of experimental measurements with the numerical breakthrough curves in a semi-logarithmic scale and b) time evolution of the mesh cardinality for three different choices of the spatial tolerance τ_h

Figure 7 compares the corresponding results with the experimental measurements. As shown in Fig. 7-a), the three simulations seem to correctly reproduce the general trend of the experimental measurements within the considered time window. However, a detailed inspection of the concentration trend at the initial times shows a significant difference among the three approximations (see Fig. 7-b, where data are plotted in a semi-logarithmic scale to emphasize the small values of the concentration characterizing the early tail of the solute breakthrough curve). Note that accurate modeling of the early solute arrivals is often crucial, for instance when dealing with risk assessment analysis in contaminant transport scenarios [2]. The data of the experiment 1 show

two isolated positive concentration values at $t < 3{,}000$s; then, a sudden increase of the concentration is observed at $t \approx 3{,}000$s. In our analysis we assume that the early arrival time of the solute can be identified with $t \approx 3{,}000$s, since the earlier values can be considered as oscillations which typically cannot be rendered by a continuum scale approximation such as the ADE (1). The solution obtained through a fixed space-time discretization under-estimates the solute early arrival time of about 400s (i.e., of about 15% of the experimental value). When the mesh is spatially adapted and the time step is fixed to $\Delta t = 1$s, the difference between the numerical and the experimental breakthrough curves significantly reduces. However, this approach is computationally expensive, since the spatial mesh is adapted at each of the $12{,}000$ time steps. The space-time adaptivity still provides a sufficiently accurate solution, while containing the whole computational cost as the total number of time steps reduces to $1{,}232$. To provide a quantitative assessment of the results, we compute the mean squared error (MSE) between the computed and the observed breakthrough concentrations depicted in Figure 7. The MSE is defined as

$$MSE = \frac{\sum_{i=1}^{N_O} \left[C_{out,h}(t_i) - C^*_{out}(t_i)\right]^2}{N_O}, \tag{28}$$

where C^*_{out} and $C_{out,h}$ are the experimentally measured and the numerically computed breakthrough concentrations, respectively, N_O is the number of available experimental observations and t_i denotes the time corresponding to the i-th observation. For the fixed uniform meshes we obtain a MSE of $6.417 \cdot 10^{-4}$. The MSE decreases to $2.983 \cdot 10^{-4}$ and $2.811 \cdot 10^{-4}$ when resorting to space and to space-time adaptive procedures, respectively. We observe that, while all three approximation strategies yield acceptable results in terms of MSE, the adaptive discretization strategies enable us to halve the MSE with respect to the fixed uniform discretization. Moreover, consistent with results presented in Section 5.1, we emphasize that the space-time discretization technique enables us to obtain a slight improvement of the accuracy with respect to the space adaptive methodology, while significantly reducing the computational cost.

Now, we assess the sensitivity of the numerical results to the tolerances, τ_h and $\tau_t^{\Delta t}$. Figure 8 compares the experimental data with the solutions associated with the three choices $\tau_h = 1$, 1.4, 1.8 for $\tau_t^{\Delta t} = 0.17$. In particular, Fig. 8-a) provides the corresponding early breakthrough curves analogously to Fig. 7-b), while Fig. 8-b) shows the evolution in time of the cardinality of the adapted meshes. The capability of the numerical breakthrough curves to reproduce experimental observations decreases as the tolerance increases while the trend becomes more and more irregular (see Fig. 8-a). In particular, the numerical curves locate leftward which means that the solute arrival time is underestimated by the numerical procedure. This can be justified by the considerable difference in terms of mesh cardinality among the three simulations, as shown in Fig. 8-b). For $\tau_h = 1$ the number of elements increases for $t \in [0, 2{,}600]$s; then, the maximum threshold $\mathcal{N}_{max} = 10{,}000$ is reached and maintained for the remaining part of the simulation time window. The increase in the number of elements is also associated with

the decrease of the parameter p_{min}, from 10^{-6}m^2 to 10^{-9}m^2, as previously discussed. For $\tau_h = 1.4$, we get a similar oscillation in the mesh cardinality for $t < 2,600$s. Nevertheless, in this case, the number of elements smoothly increases up to approximately $8,000$ triangles at the end of the simulation and the maximum number $\mathcal{N}_{max}$ of elements is never reached. For $\tau_h = 1.8$, the number of mesh elements is around $1,000$ for the entire simulation time. This significant difference with respect to the number of elements predicted for $\tau_h = 1$ is reflected in the computed breakthrough curve (Fig. 8-a). The strong oscillations exhibited by the numerical solution can be also ascribed to the reinterpolation step which involves coarse meshes for $\tau_h = 1.8$. The amplitude of the oscillations reduces for $\tau_h = 1.4$ and $\tau_h = 1$, namely in the presence of finer meshes.

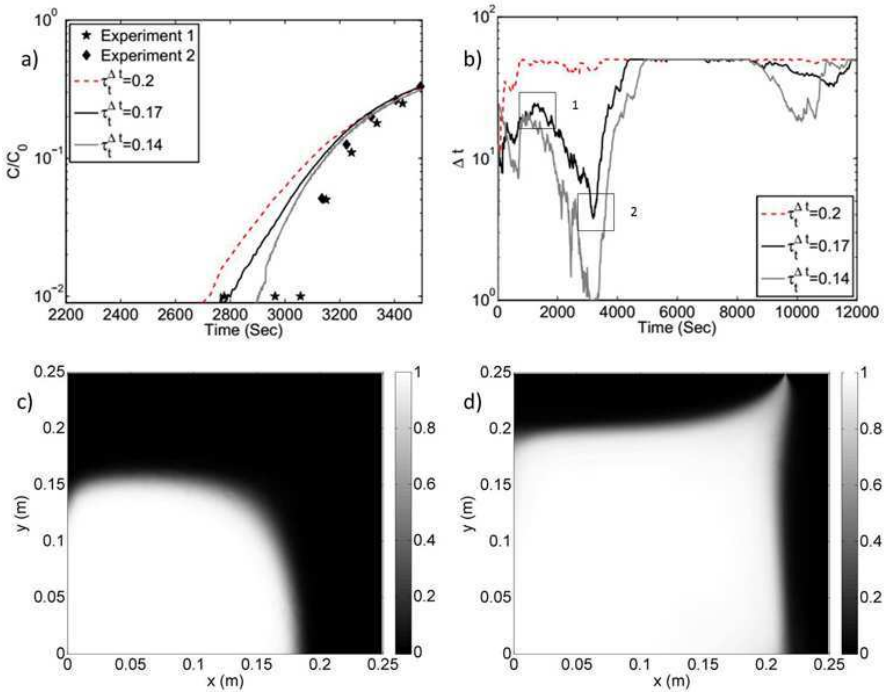

Figure 9: Experimental flow cell: a) comparison of experimental measurements with the numerical breakthrough curves in a semi-logarithmic scale and b) evolution of the time step Δt for three different choices of the local time tolerance $\tau_t^{\Delta t}$; c) concentration fields corresponding to box 1 and d) to box 2

Finally, we perform a sensitivity analysis to the local time tolerance $\tau_t^{\Delta t}$. Figure 9-a) provides a comparison among the breakthrough curves and the experimental data for $\tau_h = 0.7$ and by choosing $\tau_t^{\Delta t} = 0.14, 0.17, 0.2$. As expected, the accuracy of the numerical solution decreases as the tolerance increases. In Fig. 9-b) we show the evolution of the time step predicted for the three different choices of $\tau_t^{\Delta t}$. For $\tau_t^{\Delta t} = 0.2$, the time step quickly changes from the initial value Δt_{min} to Δt_{max} and then it remains constant for the rest of the simulation. For $\tau_t^{\Delta t} = 0.17$, the time step initially increases until reaching $\Delta t \approx 20$s at $t \approx 1,500$s. The numerical solution corresponding to this time level is

shown in Fig. 9-c). In this initial phase the concentration front has a reduced amplitude and the concentration is equal to zero in a considerable portion of the domain. At the same time, the concentration gradient at the front decreases due to the effect of dispersion. These features justify the trend of the time step observed in Fig. 9-b). As the front expands, we observe a progressive reduction of the time step,which attains a minimum value $\Delta t \approx 5$s at $t \approx 3,000$s when the solute reaches the outlet section (see Fig. 9-d), i.e., when the breakthrough curve starts to sharply increase in time. As time advances, the concentration field smoothly evolves and, for $t > 3,000$s, Δt tends to the maximum allowed value $\Delta t_{max} = 50$s. A similar trend can be observed for $\tau_t^{\Delta t} = 0.14$, even though the predicted time steps are now, in general, smaller with respect to the ones associated with $\tau_t^{\Delta t} = 0.17$. For instance, Δt reaches the minimum value $\Delta t_{min} = 1$s around $t \approx 3,000$s for a limited time interval.

6 Discussion and Concluding Remarks

Accurate numerical approximations are required to obtain reliable predictions of solute transport processes in porous media. In this paper, we detail an adaptive numerical methodology, where the computational space and time discretizations are automatically selected on the basis of a suitable error control. In particular, we implement an anisotropic mesh adaptation technique which allows us to optimize the spatial computational grid according to the directional features of the numerical solution. Both the adaptive procedures are grounded on recovery-based error estimators, which typically guarantee robust and computationally cheap error estimates.

A spatial mesh adaptivity significantly increases the accuracy of a finite element approximation for a fixed number of elements. This has been quantitatively verified in Sect. 5 by comparing the numerical results with an analytical solution as well as with experimental measurements. However, the proposed metric-based adaptive procedure may become computationally intensive, especially due to the prediction of the new metric. As a consequence, we have tried to contain the number of solution-adaptation iterations throughout each simulation, by combining space with time adaptivity. Results in Sect. 5 show that coupling mesh with time step adaptivity leads to a degree of accuracy similar to the one provided by the spatial adaptivity only, but it significantly reduces the number of demanded time steps.

The comparison against experimental data has allowed to assess the influence of the space-time discretization strategy on the accuracy of the simulation, quantified in terms of solute concentration at the outlet section (i.e., the solute breakthrough curve). In particular, we have focused on the analysis of the early solute arrival times, which are relevant in practical applications, such as risk assessment in contaminant transport analysis. It is shown that an adaptive space-time discretization is able to greatly improve the prediction of early solute arrival times with respect to a fixed uniform space-time discretization, clearly upon setting the same physical parameters in the differential problems describing flow and solute transport, respectively. This result suggests that the impact of an adaptive space-time discretization within parameter calibration and

inverse modeling schemes may be relevant in laboratory and field scale applications.

An *ad-hoc* tuning of the parameters involved in the solution-adaptation procedure proved to be a key issue in view of meaningful results. In more detail, we constrain both the space and time adaptivity via a set of criteria which improve the robustness of the solution-adaptation approach. We resort to both global and local controls, by fixing the minimum and maximum number of mesh elements and a minimum value for the element area. Our results show that these controls have to be tuned according to the characteristic space-time scales of the problem at hand, as well as to the desired accuracy. In particular, a coarse mesh typically yields an oscillating numerical breakthrough curve, due to successive interpolations between coarse meshes at the outlet section. On the contrary, when the tolerance and the minimum element area are properly tuned, these oscillations attain a negligible amplitude (i.e., $O(10^{-2})$ or smaller).

Future investigations may lead to combine different information within the space-time adaptive strategy by properly intersecting distinct metrics, as proposed, e.g., in [46]. These metrics may be related to the numerical solution as well as to a target output of the simulation (e.g., the breakthrough curve), in the spirit of a goal-oriented approach [17, 4, 25]. Further extensions of this research will involve solute transport modeling in the presence of both block heterogeneous and random permeability fields, with a view to field scale applications.

Acknowledgements

We kindly acknowledge Prof. Brian Berkowitz for sharing with us the experimental data.

References

[1] Alauzet, F., Mehrenberger, M.: P1-conservative solution interpolation on unstructured triangular meshes. Internat. J. Numer. Methods Engrg. **84**(13), 1552-1588 (2010)

[2] Andričević, R., Cvetkovic, V.: Evaluation of risk from contaminants migrating by groundwater, Water Resour. Res. **32** (3), 611-621 (1996)

[3] Bear, J., Cheng, A.H.-D.: Modeling Groundwater Flow and Contaminant Transport. Springer Dordrech (2010)

[4] Becker, R., Rannacher, R.: An optimal control approach to a posteriori error estimation in finite element methods. Acta Numerica **10**,1-102 (2001)

[5] Bouillard, P., Allard, J.-F., Warzée, G.: Superconvergent patch recovery technique for the finite element method in acoustic. Comm. Numer. Methods Engrg. **12**(9), 581-594 (1996)

[6] Brezzi, F., Fortin, M.: Mixed and Hybrid Finite Element Methods. Springer New York (1991)

[7] Brooks, A.N., Hughes, T.J.R.: Streamline upwind/PetrovGalerkin formulations for convection dominated flows with particular emphasis on the incompressible NavierStokes equations. Comput. Methods Appl. Mech. Engrg. **32** (13), 199–259 (1982)

[8] Cai, Z., Zhang, S.: Recovery-based error estimators for interface problems: mixed and nonconforming finite elements. SIAM J. Numer. Anal. **48**(1), 30-52 (2010)

[9] Cao, J., Kitanidis, P.K.: Adaptive-grid simulation of groundwater flow in heterogeneous aquifers. Adv. Water Resour. **22** (7), 681-696 (1999)

[10] Carstensen, C., Bartels, S.: Each averaging technique yields reliable a posteriori error control in FEM on unstructured grids. I: low order conforming, nonconforming, and mixed FEM, Math. Comp. **71**, 945-969 (2001)

[11] Cascón, J.M., Ferragut, L., Asensio, M.I.: Space-time adaptive algorithm for the mixed parabolic problem. Numer. Math. **103** (3), 367-392 (2006)

[12] Castro-Diaz, M.J., Hecht, F., Mohammadi, B., Pironneau, O.: Anisotropic unstructured mesh adaptation for flow simulations. Int. J. Numer. Meth. Fluids **25** (4), 475-491 (1997)

[13] Ciarlet, P.G.: The Finite Element Method for Elliptic Problems. North Holland Publishing Co., Amsterdam (1978)

[14] Clément, Ph.: Approximation by finite element functions using local regularization. RAIRO Anal. Numér. **2**, 77-84 (1975)

[15] Correa, M.R., Loula, A.F.D.: Unconditionally stable mixed finite element methods for Darcy flow. Comput. Methods Appl. Mech. Engrg. **197** (17), 1525-1540 (2008)

[16] Diersch, H.-J.: Finite element modelling of recirculating density-driven saltwater intrusion processes in groundwater. Adv. Water Resour. **11** (1), 25-43 (1988)

[17] Eriksson, K., Estep, D., Hansbo, P., Johnson, C.: Introduction to adaptive methods for differential equations. Acta Numerica **4**, 105-158 (1995)

[18] Farrell, P.E., Micheletti, S., Perotto, S.: An anisotropic Zienkiewicz-Zhu-type error estimator for 3D applications. Int. J. Numer. Meth. Eng. **85** (6), 671-692 (2011)

[19] Farrell, P.E., Piggott, M.D., Pain, C.C., Gorman, G.J., Wilson, C.R.: Conservative interpolation between unstructured meshes via supermesh construction. Comput. Methods Appl. Mech. Engrg. **198** (33-36), 2632-2642 (2009)

[20] Fetter, C.W.: Contaminant Hydrogeology, Waveland Prentice Hall (2008)

[21] Formaggia, L., Perotto, S.: New anisotropic a priori error estimates. Numer. Math. **89** (4), 641-667 (2001)

[22] Formaggia, L., Perotto, S.: Anisotropic error estimates for elliptic problems. Numer. Math. **94** (1), 67-92 (2003)

[23] Gedeon, M., Mallants, D.: Sensitivity analysis of a combined groundwater flow and solute transport model using local-grid refinement: a case study. Math. Geosci. **44** (7), 881-899 (2012)

[24] George, P.L., Borouchaki, H.: Delaunay Triangulation and Meshing: Application to Finite Elements. Hermes Paris (1998)

[25] Giles, M.B., Suli, E.: Adjoint methods for PDEs: a posteriori error analysis and postprocessing by duality. Acta Numerica **11**, 145-236 (2002)

[26] Gruau, C., Coupez, T.: 3D tetrahedral, unstructured and anisotropic mesh generation with adaptation to natural and multidomain metric. Comput. Methods Appl. Mech. Engrg. **194** (48-49), 4951-4976 (2005)

[27] Hecht, F.: New development in FreeFem++. J. Numer. Math. **20** (3-4), 251-265 (2012)

[28] Katragadda, P., Grosse, I.R.: A posteriori error estimation and adaptive mesh refinement for combined thermal-stress finite element analysis. Computers and Structures **59** (6), 1149-1163 (1996)

[29] Kavetski, D., Binning, P., Sloan, S.W.: Adaptive backward Euler time stepping with truncation error control for numerical modelling of unsaturated fluid flow. Int. J. Numer. Meth. Engng. **53** (6), 1301-1322 (2002)

[30] Knupp, P.: A moving mesh algorithm for 3-D regional groundwater flow with water table and seepage face. Adv. Water Resour. **19** (2), 83-95 (1996)

[31] Krìzek, M., Neittaanmäki, P.: Superconvergence phenomenon in the finite element method arising from average gradients, Numer. Math. **45** (1), 105-116 (1984)

[32] Levy, M., Berkowitz, B.: Measurement and analysis of non-Fickian dispersion in heterogeneous porous media. J. Contam. Hydrol. **64** (3), 203-226 (2003)

[33] Maisano, G., Micheletti, S., Perotto, S., Bottasso, C.L.: On some new recovery-based a posteriori error estimators. Comput. Methods Appl. Mech. Engrg. **195**, 4794-4815 (2006)

[34] Mansell, R.S., Ma, L., Ahuja, L.R., Bloom, S.A: Adaptive grid refinement in numerical models for water flow and chemical transport in soil. Vadose Zone J. **1** (2), 222-238 (2002)

[35] Masud, A., Hughes, T.J.R.: A stabilized mixed finite element method for Darcy flow. Comput. Methods Appl. Mech. Engrg. **191** (39), 4341-4370 (2002)

[36] Mehl, S., Hill, M.C.: Development and evaluation of a local grid refinement method for block-centered finite-difference groundwater models using shared nodes. Adv. Water Resour. **25** (5), 497-511 (2002)

[37] Meidner, D., Vexler, B.: Adaptive space-time finite element methods for parabolic optimization problems. SIAM J. Control Optim. **46** (1), 116-142 (2007)

[38] Micheletti, S., Perotto, S.: Anisotropic mesh adaption for time-dependent problems. Int. J. Numer. Methods Fluids. **58** (9), 1009-1015 (2008)

[39] Micheletti, S., Perotto, S., Farrell, P.E.: A recovery-based error estimator for anisotropic mesh adaptation in CFD. SeMA J. **50** (1), 115-137 (2010)

[40] Micheletti, S., Perotto, S., Picasso, M.: Stabilized finite elements on anisotropic meshes: a priori error estimates for the advection-diffusion and the Stokes problems. SIAM J. Numer. Anal. **41** (3), 1131-1162 (2003)

[41] Micheletti, S., Perotto, S.: Anisotropic adaptation via a Zienkiewicz-Zhu error estimator for 2D elliptic problems. In Numerical Mathematics and Advanced Applications, Springer-Verlag, Kreiss, G., Lötstedt, P., Malqvist, A, Neytcheva, M. (Eds), 645-653 (2010)

[42] Micheletti, S., Perotto, S.: Reliability and efficiency of an anisotropic Zienkiewicz-Zhu error estimator. Comput. Methods Appl. Mech. Engrg. **195** (9), 799-835 (2006)

[43] Mu, L., Jari, R.: A recovery-based error estimate for nonconforming finite volume methods of interface problems. Appl. Math. Comput. **220**, 63-74 (2013)

[44] Nakshatrala, K.B., Turner, D.Z., Hjelmstad, K.D., Masud, A.: A stabilized mixed finite element method for Darcy flow based on a multiscale decomposition of the solution. Comput. Methods Appl. Mech. Engrg. **195**(33-36), 4036-4049 (2006)

[45] Peraire, J., Vahdati, M., Morgan, K., Zienkiewicz, O.: Adaptive remeshing for compressible flow computations. J. Comput. Phys. **72** (2), 449-466 (1987)

[46] Porta, G.M., Perotto, S., Ballio, F.: Anisotropic mesh adaptation driven by a recovery-based error estimator for shallow water flow modeling. Int. J. Numer. Methods Fluids. **70** (3), 269-299 (2012)

[47] Porta, G.M., Perotto, S., Ballio F.: A space-time adaptation scheme for unsteady shallow water problems. Math. Comput. Simulat. **82** (12), 2929-2950 (2011)

[48] Rodríguez, R.: Some remarks on Zienkiewicz-Zhu estimator, Numer. Methods Partial Differential Equations **10**, 625-635 (1994)

[49] Saaltink, M.W., Carrera, J., Olivella S.: Mass balance errors when solving the convective form of the transport equation in transient flow problems. Water Resour. Res., **40** (5), W05107, doi:10.1029/2003WR002866 (2004)

[50] Schmich, M., Vexler, B.: Adaptivity with dynamic meshes for space-time finite element discretizations of parabolic equations. SIAM J. Sci. Comput. **30** (1), 369-393 (2008)

[51] Sun, S., Wheeler, M.F.: Anisotropic and dynamic mesh adaptation for discontinuous Galerkin methods applied to reactive transport. Comput. Methods Appl. Mech. Engrg. **195** (25), 3382-3405 (2006)

[52] Wexler, E.J.: Analytical Solutions for One-, Two-, and Three-Dimensional Solute Transport in Ground-Water Systems with Uniform Flow. U.S. Geological Survey, Techniques of Water-Resources Investigations, Book **3**, Chapter 7 (2005)

[53] Yan, N.N., Zhou, A.: Gradient recovery type a posteriori error estimates for finite element approximations on irregular meshes. Comput. Methods Appl. Mech. Engrg. **190** (32), 4289-4299 (2001)

[54] Younes, A., Ackerer, P., Lehmann, F.: A new efficient Eulerian-Lagrangian localized adjoint method for solving the advection-dispersion equation on unstructured meshes. Adv. Water Resour. **29** (7), 1056-1074 (2006)

[55] Younes, A., Ackerer, P.: Empirical versus time stepping with embedded error control for density-driven flow in porous media. Water Resour. Res., **46** (8), W08523, doi:10.1029/2009WR008229 (2010)

[56] Zienkiewicz, O.C., Zhu, J.Z.: A simple error estimator and adaptive procedure for practical engineerng analysis. Int. J. Numer. Meth. Eng. **24** (2), 337-357 (1987)

[57] Zienkiewicz, O.C., Zhu, J.Z.: The superconvergence patch recovery and a posteriori error estimates, Part 1: The recovery technique. Int. J. Numer. Methods Eng. **33** (7), 1331-1364 (1992)

[58] Zienkiewicz, O.C., Zhu, J.Z.: The superconvergence patch recovery and a posteriori error estimates, Part 2: Error estimates and adaptivity. Int. J. Numer. Methods Eng., **33** (7), 1368-1382 (1992)

MOX Technical Reports, last issues

Dipartimento di Matematica "F. Brioschi",
Politecnico di Milano, Via Bonardi 9 - 20133 Milano (Italy)

15/2014 Bahman Esfandiar, Giovanni Porta, Simona Perotto, Alberto Guadagnini
Anisotropic mesh and time step adaptivity for solute transport modeling in porous media

14/2014 Dassi, F.; Formaggia, L.; Zonca, S.
Degenerate Tetrahedra Recovering

13/2014 Ballarin, F.; Manzoni, A.; Quarteroni, A.; Rozza, G.
Supremizer stabilization of POD-Galerkin approximation of parametrized Navier-Stokes equations

12/2014 Fumagalli, I; Parolini, N.; Verani, M.
Shape optimization for Stokes flow: a reference domain approach

11/2014 Taddei, T.; Quarteroni, A.; Salsa, S.
An offline-online Riemann solver for one-dimensional systems of conservation laws

10/2014 Antonietti, P.F.; Dedner, A.; Madhavan, P.; Stangalino, S.; Stinner, B.; Verani, M.
High order discontinuous Galerkin methods on surfaces

09/2014 Chen, P.; Quarteroni, A.
A new algorithm for high-dimensional uncertainty quantification problems based on dimension-adaptive and reduced basis methods

08/2014 Cattaneo, L; Zunino, P.
A computational model of drug delivery through microcirculation to compare different tumor treatments

07/2014 Agasisti, T.; Ieva, F.; Paganoni, A.M.
Heterogeneity, school-effects and achievement gaps across Italian regions: further evidence from statistical modeling

06/2014 Benzi, M.; Deparis, S.; Grandperrin, G.; Quarteroni, A.
Parameter estimates for the relaxed dimensional factorization preconditioner and application to hemodynamics